



Whole-genome characterization of chronological age-associated changes in methylome and circular RNAs in moso bamboo (*Phyllostachys edulis*) from vegetative to floral growth

Zeyu Zhang^{1,†}, Huihui Wang^{1,†}, Yongsheng Wang^{2,†}, Feihu Xi^{2,†}, Huiyuan Wang¹, Markus V. Kohnen¹, Pengfei Gao¹, Wentao Wei¹, Kai Chen², Xuqing Liu¹, Yubang Gao², Ximei Han¹, Kaiqiang Hu¹, Hangxiao Zhang¹, Qiang Zhu¹ , Yushan Zheng³, Bo Liu³, Ayaz Ahmad⁴, Yau-Heiu Hsu⁵, Steven E. Jacobsen^{6,*} and Lianfeng Gu^{1,*} 

¹Basic Forestry and Proteomics Research Center, College of Forestry, Fujian Provincial Key Laboratory of Haixia Applied Plant Systems Biology, Fujian Agriculture and Forestry University, Fuzhou 350002, China,

²Basic Forestry and Proteomics Research Center, College of life science, Fuzhou 350002, China,

³College of Forestry, Fujian Agriculture and Forestry University, Fuzhou 350002, China,

⁴Department of Biotechnology, Abdul Wali Khan University Mardan, Mardan, Pakistan,

⁵Graduate Institute of Biotechnology, National Chung Hsing University, Taichung, Taiwan, and

⁶Department of Molecular, Cell & Developmental Biology, Howard Hughes Medical Institute, University of California, Los Angeles, CA 90095, USA

Received 29 October 2020; revised 30 December 2020; accepted 5 January 2021.

*For correspondence (e-mail jacobsen@ucla.edu and lfgu@fafu.edu.cn).

[†]These authors contributed equally to this work.

SUMMARY

In mammals, DNA methylation is associated with aging. However, age-related DNA methylation changes during phase transitions largely remain unstudied in plants. Moso bamboo (*Phyllostachys edulis*) requires a very long time to transition from the vegetative to the floral phase. To comprehensively investigate the association of DNA methylation with aging, we present here single-base-resolution DNA methylation profiles using both high-throughput bisulfite sequencing and single-molecule nanopore-based DNA sequencing, covering the long period of vegetative growth and transition to flowering in moso bamboo. We discovered that CHH methylation gradually accumulates from vegetative to reproductive growth in a time-dependent fashion. Differentially methylated regions, correlating with chronological aging, occurred preferentially at both transcription start sites and transcription termination sites. Genes with CG methylation changes showed an enrichment of Gene Ontology (GO) categories in 'vegetative to reproductive phase transition of meristem'. Combining methylation data with mRNA sequencing revealed that DNA methylation in promoters, introns and exons may have different roles in regulating gene expression. Finally, circular RNA (circRNA) sequencing revealed that the flanking introns of circRNAs are hypermethylated and enriched in long terminal repeat (LTR) retrotransposons. Together, the observations in this study provide insights into the dynamic DNA methylation and circRNA landscapes, correlating with chronological age, which paves the way to study further the impact of epigenetic factors on flowering in moso bamboo.

Keywords: *Phyllostachys edulis*, epigenetic clock, DNA methylation, bisulfite sequencing, single-molecule nanopore DNA sequencing, circular RNA sequencing.

INTRODUCTION

DNA methylation is one of the major types of epigenetic modification in plants and animals, contributing to the regulation of gene expression, cell differentiation, genomic imprinting and genome integrity. During development, methylation marks can be inherited from the previous

generation, but also dynamically change in response to nutrition or environmental stress. Aging has also been associated with the gain and loss of methyl groups in different parts of the genome (Niederhuth *et al.*, 2016; Zampieri *et al.*, 2015). In plants, methylated cytosine, known as 5-methylcytosine (5mC), occurs in three different sequence contexts, derived from distinct enzymatic pathways:

symmetrical 'CG' sites, partial symmetrical 'CHG' sites (where H = A, T or C) and 'CHH' sites. The methyltransferases, chromo methyltransferases and domains rearranged methyltransferases are responsible for maintaining methylation within CG (Singh *et al.*, 2008), CHG and CHH (Pavlopoulou and Kossida, 2007) sites, respectively. Four 5mC DNA glycosylases (ROS1, DME, DML2 and DML3) demonstrate DNA demethylation activity (Zhu, 2009). 5mC is quite distinct from conventional cytosine and shows resistance to deamination by bisulfite treatment, which was developed to explore the 5mC landscape (Susan *et al.*, 1994). Whole-genome bisulfite sequencing (BS-Seq) is regarded as the gold standard for obtaining genome-wide methylation profiles (Miura *et al.*, 2012). In addition to BS-Seq, the Oxford Nanopore Technologies (ONT) sequencer can also directly identify 5mC by the detection of electrical current signals (Simpson *et al.*, 2017).

Alternative splicing (AS) and alternative polyadenylation (APA) are two important post-transcriptional modifications (Wachter *et al.*, 2007; Zhao *et al.*, 2019). AS can couple transcriptional elongation in response to environmental cues (Godoy Herz *et al.*, 2019). For example, both DNA-binding factor CTCF (Shukla *et al.*, 2011) and multifunctional protein MeCP2 (Maunakea *et al.*, 2013) regulate AS by modulating the elongation rate of RNA polymerase II (Maor *et al.*, 2015). DNA methylation cross-talks with histone H3K9 trimethylation (H3K9me3) (Du *et al.*, 2015). H3K9me3 is the binding signal for the HP1 protein, which affects the binding of splicing factors to chromatin (Yearim *et al.*, 2015). This suggests that DNA methylation might regulate AS by modulating the structure of chromatin. For instance, a study in *Oryza sativa* (rice) revealed that the null mutant of CG methyltransferase *OsMet1-2* had a genome-wide impact on AS (Wang *et al.*, 2016). Transposable elements (TEs) regulate APA by residing in the unusually large introns of *FLC* (Liu *et al.*, 2004) and *IBM1* (Rigal *et al.*, 2012). The prevalence of AS and APA in *Phyllostachys edulis* (moso bamboo) was revealed by both mRNA sequencing (RNA-Seq) (Li *et al.*, 2016) and Pacific BioSciences (PacBio) single-molecule real-time (SMRT) long-read isoform sequencing (Iso-Seq) (Wang *et al.*, 2017).

In addition to DNA methylation, circular RNAs (circRNAs) represent another layer of epigenetic regulation (Wu *et al.*, 2019) and can regulate AS (exon skipping) (Conn *et al.*, 2017). CircRNAs are long-strand covalently closed non-coding RNAs generated by back-splicing (Jeck *et al.*, 2013). CircRNAs are resistant to exonuclease-mediated degradation, and can thus serve as biomarkers (Vo *et al.*, 2019). In plants, circRNAs have been reported in *Arabidopsis thaliana* (Chen *et al.*, 2017; Zhang *et al.*, 2019b), *O. sativa* (Lu *et al.*, 2015a), *P. edulis* (Wang *et al.*, 2019) and *Zea mays* (maize) (Chen *et al.*, 2018; Zhang *et al.*, 2019a). However, an association of methylation and circRNA biogenesis has not been reported.

Several studies in humans have shown that DNA methylation can predict chronological age (Hannum *et al.*, 2013) and that DNA methylation age could be used as a biomarker of aging (Christiansen *et al.*, 2016). The mechanisms of aging have mostly been investigated in animals (Vijg and Suh, 2013). In plants, phase transitions and senescence have been reported to be under the control of DNA methylation (Ay *et al.*, 2014; Dubrovina and Kiselev, 2016; Humbeck, 2013). The relationship between DNA methylation and aging has been investigated in *A. thaliana* (Ogneva *et al.*, 2016). Moso bamboo is a large woody bamboo that has ecological, economic and cultural value in Asia, and accounts for approximately 70% of total bamboo growth area (Peng *et al.*, 2013). Methylation-sensitive amplification polymorphism (MSAP) revealed that the total DNA methylation level varies with chronological age in moso bamboo (Yuan *et al.*, 2014). However, MSAP is limited to the detection of methylation at the restriction sites of the endonuclease enzymes used. Thus, the MSAP method could not reveal DNA methylation in the level of single-base resolution. Despite the crucial roles of DNA methylation in aging and flowering, the genome-wide DNA methylation landscape of moso bamboo has not been characterized. Thus, the links between aging and DNA methylation or flowering still await exploration in moso bamboo.

To better understand how aging-related epigenetic changes correlate with phase transition and flowering during the extended developmental period of bamboo, we employed BS-Seq, single-molecule nanopore DNA sequencing, RNA-Seq, small RNA sequencing and circular RNA sequencing (circRNA-Seq). Comparing methylation levels from the young seedling stage to the flowering stage, we revealed a dynamic landscape associated with aging-related epigenetic changes in a time-dependent fashion, which provides an unprecedented opportunity to investigate the underlying mechanisms in the future. Finally, circRNA-Seq revealed hypermethylation in flanking intron regions of circRNAs, suggesting that DNA methylation might affect the biogenesis of circRNAs. To the best of our knowledge, this is the first genome-wide investigation of single-base-resolution DNA methylation and circRNAs covering a long period of lifespan in moso bamboo. This study will facilitate the investigation of DNA methylation and circRNA features related to aging and flowering, which will be valuable for understanding the molecular mechanisms of flowering control in moso bamboo.

RESULTS

Distinct morphology and cytology during phase transition

Woody bamboos are long-lived monocarpous plants with a long vegetative phase before flowering (Lin *et al.*, 2010; Numata, 1970). To investigate changes in methylation during aging in moso bamboo, we collected leaves from

3-week-old seedlings (TW), 1-year-old plants (OY), plants that will flower in the next year (FLNY), flowering plants (FL) and flower florets (FP) (Figure 1a). The leaves of FLNY turned to deeper and darker shades of green, and the chlorophyll content was lower in FL (Figure 1b). This result revealed that the leaves of OY presented the maximum size of bulliform cells and arm cells (Figure 1c; Figure S1). Cross sections of mesophyll tissue revealed that the leaves of OY and FLNY were thicker than the leaves of TW and FL (Figure 1d). Cross sections of mesophyll tissue also revealed that the leaves of FLNY were thickest, which might reinforce photosynthesis and energy storage for flowering next year (Figure S1). The trichomes on the abaxial epidermis were clearly observed in the early developmental period (TW and OY). However, most of them disappeared in the late growth stage (FL and FLNY) (Figure 1d). OY had the largest midrib, whereas TW had the smallest midrib (Figure 1e), which was consistent with the leaf size. Scanning electron microscopy analysis revealed that the trichomes on leaf edges were small and densely distributed in TW and OY, but became longer and sparser in FLNY and FL (Figure 1f,g). Flower panicles were visible on branches of moso bamboo in the bloom stage (Figure 1h). Florets grew in the flower panicle, the stamens and developing embryo were protected by glumes, and anthers were covered by the epidermis cells of the stamen (Figure 1i–n).

Genome-wide profiling of DNA methylation during phase transition

To study chronological age-associated methylation changes in moso bamboo, we performed bisulfite conversion with the EZ DNA Methylation-Gold kit (Zymo Research, <https://www.zymoresearch.com>). BS-Seq libraries were sequenced with a genome coverage of about 30× (Figure S2). The overall average CG methylation was 79.7, 81.3, 80.7, 80.7 and 80.8% for TW, OY, FLNY, FL and FP, respectively. CHG methylation was 62.2, 63.5, 63.2, 63.5 and 64.0% for TW, OY, FLNY, FL and FP, respectively. CHH methylation was 2.5, 3.1, 3.1, 3.7 and 3.2% for TW, OY, FLNY, FL and FP, respectively. The Spearman's correlation coefficient for CG was the highest, followed by CHG and CHH, which suggested that methylation at CG and CHG was more stable than that at CHH among different stages (Figures 2a and S3).

Transposable elements are hypermethylated

Hypermethylation in TEs is important for genome stability in plants. CG methylation in TEs was close to an average of 90% (Figure 2b). The distribution of CG methylation within TE regions was relatively even. CHG methylation formed a slight bulge towards the center and CHH methylation marks were slightly more frequent towards the TE transcription start sites (TSSs) and transcription

termination sites (TTSs) (Figure 2b). The distance between adjacent TEs was significantly negatively correlated with methylation levels in the intergenic region (Figure S4).

In addition to pericentromeric heterochromatin regions, TEs are also dispersed in gene-rich regions, which might influence the expression of neighboring genes (Penterman *et al.*, 2007; Zhang *et al.*, 2018). Thus, we explored methylation profiles specifically for TEs adjacent to coding genes (Figure 2c). For this type of TE, CG and CHG methylation in TE body regions was similar to the overall profile. However, there were obvious differences on either side of TE body regions. CG and CHG methylation close to flanking gene-coding regions showed a sharp drop (Figure 2c), which might reflect the action of DNA glycosylases that help avoid hypermethylation in coding genes (Penterman *et al.*, 2007). CHH methylation levels in TE body regions were higher at the end closest to the neighboring gene (Figure 2c). The levels of all three methylation types in the flanking intergenic region closest to the coding gene were lower than in the flanking intergenic region furthest away. CHH methylation in this type of TE also showed gradual aging-associated accumulation (Figure 2c).

DNA methylation profile of coding genes

CG methylation in annotated coding genes dropped towards the TSS, covered the gene body in a bell-shaped manner and increased again downstream of the TTS (Figure 2d). The overall coverage of CG methylation was approximately 48%. The CHG methylation level presented a negative bell shape along the transcriptional region. However, CHG methylation marks were asymmetrically distributed with higher levels at the TSS than at the TTS (Figure 2d). CHH methylation exhibited a concave pattern in gene bodies (Figure 2d). CHH methylation in the promoter region and at the TSS was higher than that downstream of the TTS. CHH methylation in coding genes also accumulated over time from vegetative to reproductive growth stages (Figure 2d), which is consistent with a case study in the *ITS* DNA region in *A. thaliana* (Ogneva *et al.*, 2016). A comparison of cytosine methylation from long terminal inverted repeats immediately adjacent to the *mudra* region in maize also revealed that mature leaf 6 was more methylated than immature leaf 6 (Li *et al.*, 2010).

Validation of methylation profiles with single-molecule nanopore DNA sequencing

To validate DNA methylation profiles from the gold-standard BS-Seq, we applied the MinION™ portable single-molecule nanopore sequencer to TW and FL libraries. The Spearman's correlation coefficient for CG methylation between both methods was 87 and 90% for TW and FL libraries, respectively (Figure 2e). The distribution of CG and CHG methylation from BS-Seq was similar to that from single-molecule nanopore DNA sequencing

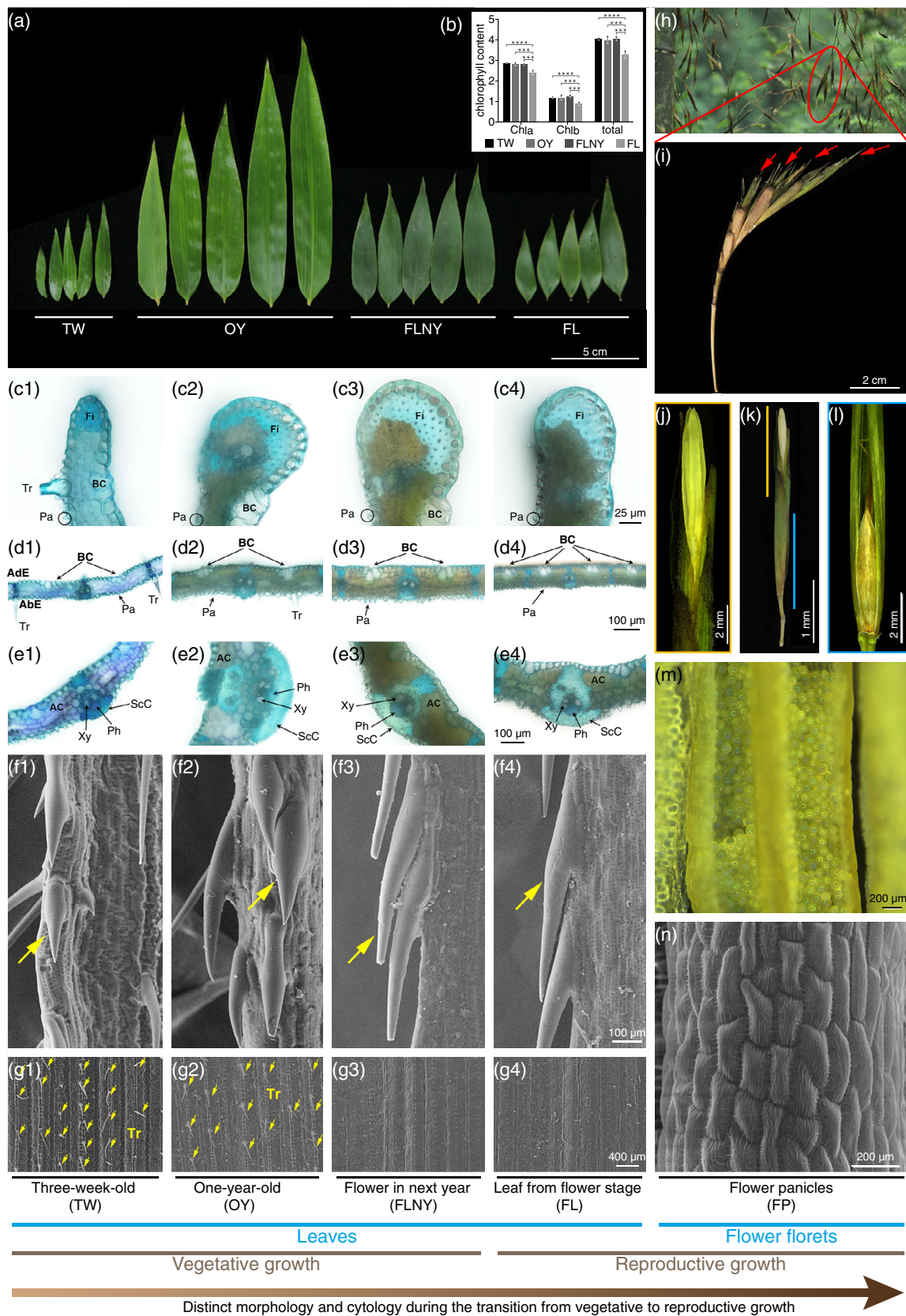


(Figure 2f). Most methylation sites identified from BS-Seq were confirmed by single-molecule nanopore DNA sequencing, which validated the accuracy of the BS-Seq sequencing (Figure 2g). It should be noted that we validated BS-Seq using single-molecule nanopore DNA sequencing by sequencing only about 2× the coverage of the bamboo genome. In this study we identified DNA methylation using BS-Seq, which is the gold standard for measuring CG, CHG and CHH methylation. Thus, we sequenced three biological repeats for BS-Seq and covered more than 90× coverage of moso bamboo genome for each stage. All of the downstream analysis in this study was based on the BS-Seq analysis.

Differential DNA methylation occurs preferentially at the TSS and the TTS

Differentially methylated regions (DMRs) between samples of consecutive chronological age revealed the gain and loss of methylation marks during development. Many DMRs lost CG methylation between the early stages of TW and OY (Figure 3a). CHG methylation remained relatively stable in leaf samples but was higher in FP than in FL (Figure 3a). For CHH methylation, most DMRs gained methylation for all pairwise comparisons. Between the early TW and OY samples, the CHH methylation marks almost doubled (Figure 3a). Interestingly, the numbers of CG-DMRs increased between OY and FLNY and subsequently remained stable, whereas the CHG-DMRs increased and subsequently decreased in numbers (Figure 3b). CHH-DMRs also accumulated over time, starting earlier than CHG-DMRs. CHH-DMRs also showed the biggest tissue-specific difference (Figure 3b). In most cases, the number of genes with CHH-DMRs was higher than the number with CHG- or CG-DMRs (Figure 3c). However, pair-wise comparison of OY and FLNY revealed that the number of genes containing CG-DMRs was roughly equal to that of genes with CHG- and CHH-DMRs (Figure 3c).

By comparing TW with other samples (FLNY, FL and FP), we found that CG- and CHG-DMRs have a higher tendency

to gain or lose methylation in both TSSs and TTSs than in the middle region of the transcript. CHG-DMRs were higher in TSS than in TTS. CG- and CHG-DMR gained methylation presented similar proportions with that of lost methylation (Figure 3d). For the comparison of TW with OY, CG- or CHG-DMRs could hardly be detected and DMR-CHHs were most frequently located around the TSS and TTS regions. However, CHH-DMRs in TSSs had a greater tendency to gain methylation than CHH-DMRs in TTSs (Figure 3d).

The DMR analysis only measured regions in 100-bp bins. To investigate global DNA methylation changes for each gene containing at least one DMR region, we calculated the correlation among pairwise comparisons using 20-bp bins covering whole gene bodies and 500 bp upstream (Figure 3e). Six 3D scatter plots presented the correlation of gained and lost methylation for CG, CHG and CHH, respectively. The correlation for CG methylation was the highest and the correlation for CHH methylation was again the lowest, consistent with the profile results. Bins in each 3D scatter plot were classified into six categories using *K*-means clustering according to correlation coefficient value, which ranged between −0.2 and 1.0 (Figure 3e). We selected the low-correlation category, which represented the most obvious methylation changes for GO term enrichment analysis. We found a significant enrichment of genes with the GO term 'vegetative to reproductive phase transition of meristem' (Figure S5). For example, these genes included CG gain genes (*PH01000696G0040* and *PH01002436G0190*) and CG loss genes (*PH01000943G0560*, *PH01000732G0370* and *PH01001722G0270*), which were associated with phase transition and showed dramatic DNA methylation changes. Among them, the methylation levels of *PH01000696G0040* in the gene body and 3' downstream of TTS changed dramatically during the phase transition (Figure 3f).

Differential gene expression during phase transition in moso bamboo

Next, we used strand-specific RNA-Seq to investigate gene expression at the four stages as well as in flower florets.

Figure 1. Distinct morphology and cytology of leaves and flower florets of *Phyllostachys edulis* (moso bamboo) during the transition from vegetative to reproductive growth.

- (a) Phenotype of leaves at four distinct growth stages of moso bamboo.
- (b) Chlorophyll levels at four distinct growth stages of moso bamboo.
- (c) Transverse section of leaf edges.
- (d) Transverse section of the middle of leaves.
- (e) Transverse section of primary leaf veins.
- (f) Scanning electron microscope images of trichomes (yellow arrows) on the leaf edge.
- (g) Scanning electron microscope images of trichomes (yellow arrows) on the leaf.
- (h) Flowering under natural conditions.
- (i) Flower panicle, indicated by the red ellipse in (h).
- (j) Microscope observation of a single floret, indicated by a yellow line in (k).
- (k) A single floret, indicated by red arrows in (i).
- (l) A seed has begun to develop at the bottom of the single floret, indicated by a blue line in (k).
- (m) Microscopy of pollen.
- (n) Scanning electron microscope images of epidermal cells of a floret. Abbreviations: AbE, abaxial epidermis; AC, arm cells; AdE, adaxial epidermis; BC, bulliform cells; Fi, fibers; Pa, papillae; Ph, phloem; Pr, prickles; ScC, sclerenchyma cell; Tr, trichome; Xy, xylem.

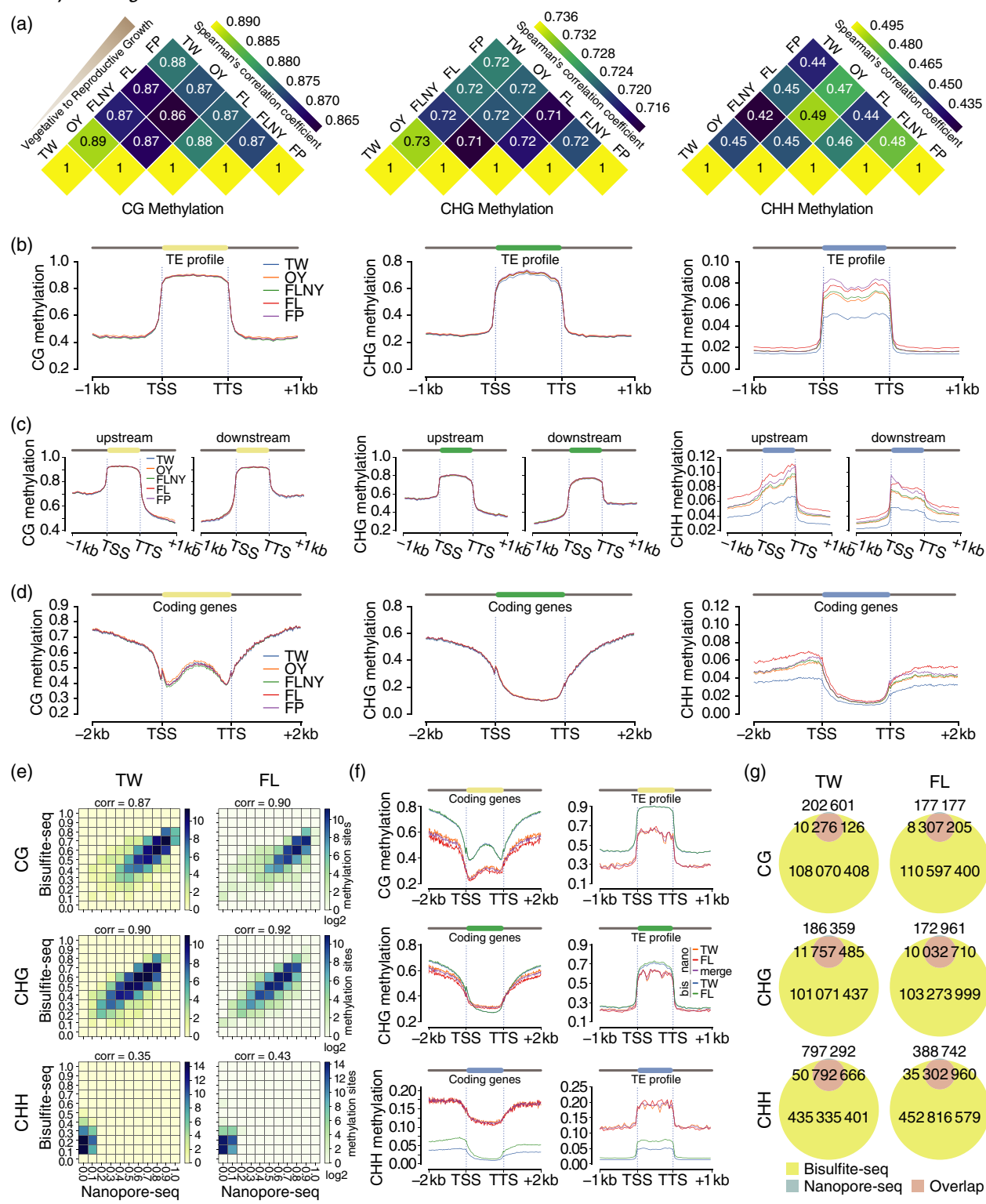


Figure 2. Genome-wide methylation profile based on bisulfite sequencing (BS-Seq) and Nanopore single-molecule DNA sequencing.

- (a) Correlation of CG, CHG and CHH methylation among different samples.
 (b) Global DNA methylation landscape in transposable elements (TEs).
 (c) Global DNA methylation landscape in TEs located up- or downstream of annotated genes.
 (d) Global DNA methylation landscape in coding genes.
 (e) Correlation between BS-Seq and Nanopore single-molecule DNA sequencing.
 (f) The distribution of methylation in genes and TEs based on both BS-Seq and single-molecule DNA sequencing.
 (g) Venn diagrams of methylation sites identified by BS-Seq and single-molecule nanopore DNA sequencing.

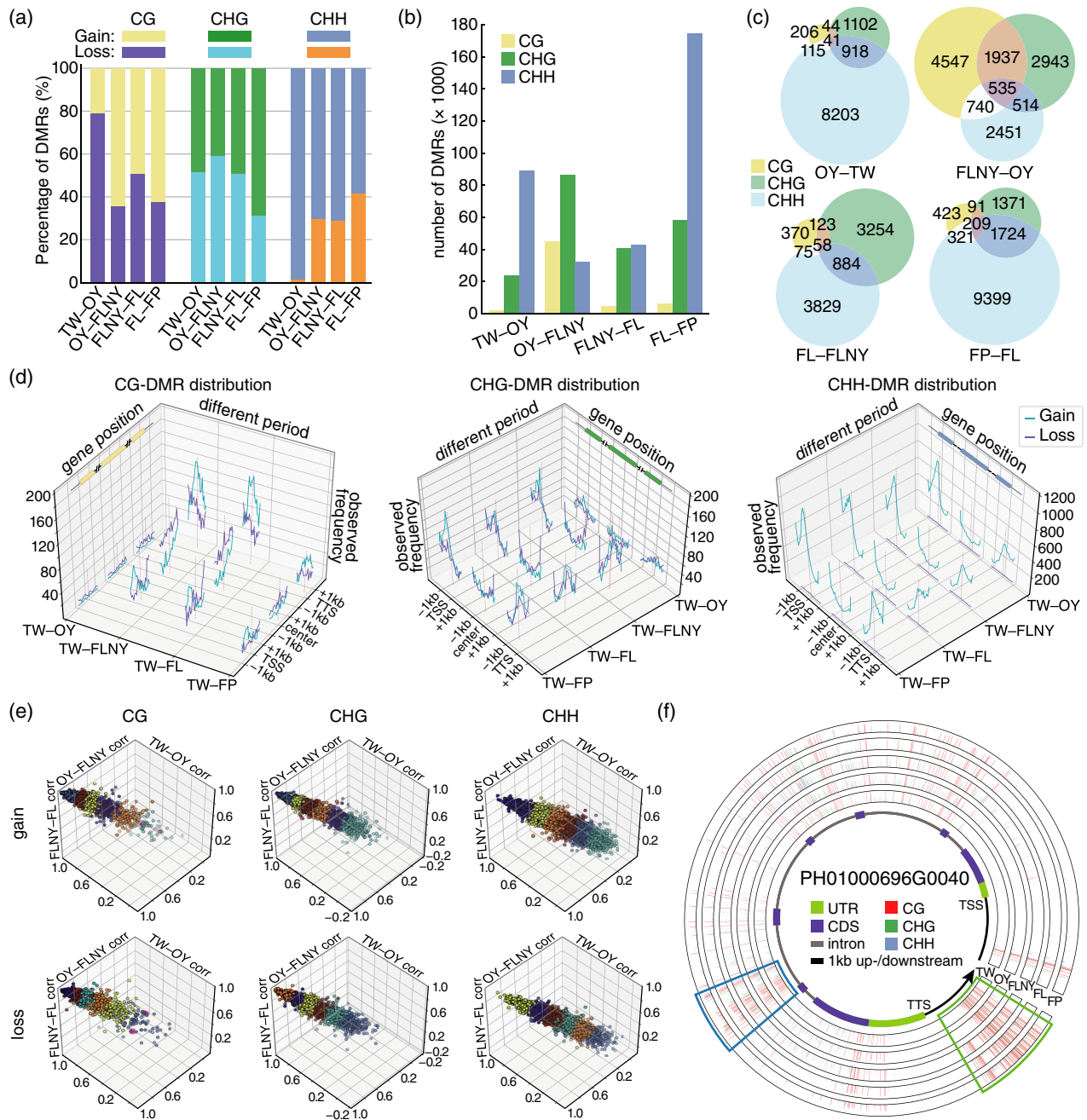


Figure 3. Genome-wide differential DNA methylation profile.

(a) The percentage of differentially methylated regions (DMRs) gained or lost between consecutive periods.

(b) Overall numbers of DMRs.

(c) Comparison of DMR-containing genes.

(d) DMR distribution along TE transcription start sites (TSSs), central gene body and transcription termination sites (TTSs), based on pairwise comparisons.

(e) Gene body, together with upstream and downstream 1 kb, were used for the calculation of methylation with 20-nt bins. The number of clusters was chosen to be $n_{clusters} = 6$, and the points were plotted in the graph using 3D graphs.

(f) Wiggly plot showing differential methylation in gene body and downstream region of the *PH01000696G0040* locus.

First, we investigated all genes with functions related to 'vegetative to reproductive phase transition' and clustered them into three major groups based on their expression levels (Figure S6). Genes in the first cluster (blue) showed

low expression in leaves and either continuously low or upregulated transcript levels in FP, suggesting that the blue cluster comprises tissue-specifically regulated genes. The yellow cluster contains genes with low expression in

young leaves (TW) and moderately upregulated expression in older tissues (OY–FP). The third cluster (orange) comprises consistently highly expressed genes from as early as the TW seedling stage. However, some of these genes showed a downward trend in FP (Figure S6). Then, we identified significantly differentially expressed genes between consecutive samples sorted by age. GO enrichment analysis of all these differentially expressed genes revealed GO terms related to reproductive developmental processes in both down- and upregulated genes (Figure S7).

To reveal the most relevant module of highly related genes, we performed weighted correlation network analysis (WGCNA) for genes with differential expression. Several distinct co-expression modules in the hierarchical cluster tree were summarized using the module eigen-genes (Figure S8). For each sample, there was at least one module that correlated with upregulation at only one particular stage (Figure S9). The red and blue modules were relevant to TW and OY, respectively, and were enriched in ‘photosynthesis’ (red) and ‘phototransduction’ and ‘nuclear mRNA 5’ splicing site recognition’ (blue). The black module was relevant to FLNY and was enriched in ‘reproduction cellular process’. A previous study reported that soil nitrogen and exchanged Ca and Mg content showed a reduction in sites after bamboo mass flowering and death, in

comparison with regions in living bamboo (Takahashi *et al.*, 2007). Consistent with this, the FL period (green module) was enriched in ‘regulation of nutrient levels in leaf’ (Figure S9).

To further identify hub genes, we selected genes that were differentially expressed and had DMR from leaves as potential candidates for being involved in the regulation of methylation-related gene expression during aging using WGCNA (Langfelder and Horvath, 2007). The top 10% of the most relevant gene pairs were selected based on the gene expression and methylation levels. The important hub genes were identified from the overlapping genes (Figure 4a), which were likely to be involved in aging. In total, we identified 59, 113 and 136 important genes for CG, CHG and CHH, respectively (Figure 4b). GO enrichment analysis for these genes revealed GO enrichment terms, including RNA methylation, RNA modification, RNA processing, protein import, protein localization, ribosome biogenesis and cell cycle checkpoint (Figure S10).

Methylation in promoter region correlates with gene expression

We further investigated the relationship between gene expression and methylation in promoter sequences. CG methylation was the predominant methylation type prone to hypermethylation or hypomethylation (Figure S11).

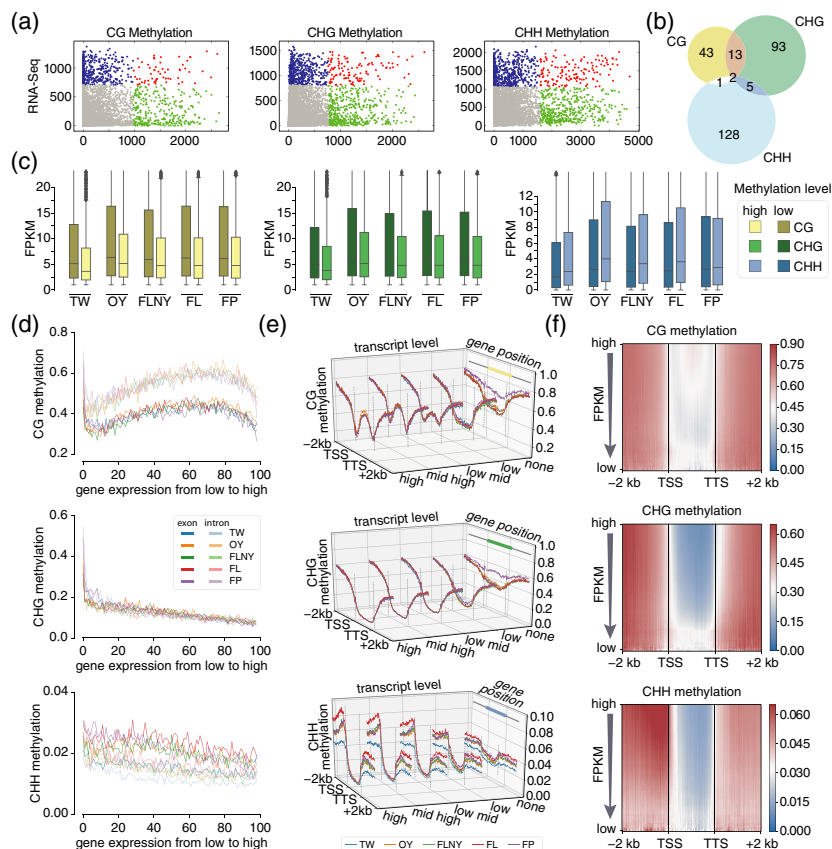


Figure 4. DNA methylation and gene expression. (a) Hub-gene network between DNA methylation and gene expression. The nodes above the 90th percentile for the number of edges were defined as the hub nodes in each co-expression network. (b) Venn diagram of important hub genes for CG, CHG and CHH. (c) Distribution of expression level of genes with high or low methylation in promoter regions. (d) Methylation profiles in exons or introns of genes with different expression levels. The intron-including genes were grouped into 100 subsets (x-axis) according to expression level from low to high. The y-axis shows the methylation levels for CG, CHG and CHH. (e) Methylation profiles in promoter and gene-body regions of genes with different expression levels. The intron-including genes were grouped into different subsets according to expression level, from low to high. The y-axis shows methylation levels for CG, CHG and CHH. (f) Heatmap representation of CG, CHG and CHH methylation profiles in genes from low to high expression groups.

Indeed, genes with hypomethylated promoter sequences were more strongly expressed than those with highly methylated promoters (Figure 4c), which is consistent with the known inhibitory effect of hypermethylation on gene expression. CHG methylation showed a similar methylation pattern to CG but had a higher proportion of hypomethylation. By contrast, high CHH methylation levels in promoters were correlated with higher expression levels than genes with low CHH methylated promoters. This suggests that CHH methylation in promoter regions may positively impact gene expression (Figure 4c), which is consistent with CHH islands exhibiting positive correlation with expression level in maize (Gent *et al.*, 2013; Hsu *et al.*, 2017; Li *et al.*, 2015). A second possibility is that changes in gene expression positively impact CHH methylation levels.

CHH methylation was associated with abundance of 24-nt siRNA

In plants, small interfering RNAs (siRNAs) can guide *de novo* methylation by RNA-directed DNA methylation (RdDM) (Law and Jacobsen, 2010) in the context of the CHH sequence (Gent *et al.*, 2013). In order to explain the increased levels of CHH with chronological aging, we performed small RNA sequencing for five different samples with three biological repeats. After trimming adapter sequences, we aligned these small RNA reads with a reference genome and plotted the general trend of 24-nt siRNA distribution within an approximately 1 kb region upstream of TSS and downstream of TTS, which presented a similar profile as that of CHH (Figure S12). In particular, the CHH methylation levels (low, mid-low, mid-high, high) were associated with the abundance of 24-nt siRNAs in TW, OY, FLNY, FL and FP, respectively (Figure S12). The level of 24-nt siRNAs also showed gradual aging-associated accumulation in this order: TW, OY and FLNY. This result suggests that the gradual aging-associated accumulation of 24-nt siRNAs might partly contribute to the accumulation of CHH in chronological aging by the RdDM pathway. However, the whole level of 24-nt siRNAs in flowering samples was lower than that of FLNY. Asymmetric CHH methylation is maintained by DNA methyltransferase *DRM2* (Chan *et al.*, 2005). RNA-Seq and quantitative real-time PCR revealed that *DRM2* increased in flowering samples (Figure S13), which suggested that the increased level of CHH in flowering samples might have been caused by the upregulated expression of *DRM2*.

CG methylation level is higher in introns than in exons

We investigated the correlation between DNA methylation in exons and introns and gene expression. We divided all expressed intron-containing genes into 100 equal parts according to expression level in incremental order. We then plotted the relationship between DNA methylation in intron/exon and gene expression (Figure 4d). First, CG

methylation in introns was higher than that in exons. We investigated the percentage of CG nucleotides in intron-containing genes according to the reference sequence and gene annotation. In total, there were 3 611 812 and 1 406 368 CGs in exons and introns, respectively (Figure S14). After normalization according to the total length, the number of CG nucleotides per 1 kb were 48 and 23 for exons and introns, respectively (Figure S14). Although the number of total and methylated CG in exons was higher than that in introns, the methylation level in introns was higher than that in exons (Figure 4d). Second, CG methylation was highest for unexpressed genes. Third, CG methylation in introns or exons increased with increasing gene expression. However, for highly expressed genes at roughly the 80th centile (x-axis), the CG methylation level decreased again in both introns and exons. The CHG methylation in introns and exons was indistinguishable and decreased with increasing gene expression levels (Figure 4d). Of the three methylation types, CHH methylation in introns or exons was the lowest, although slightly higher in exons. The linear relationship between CHH methylation level and expression levels was similar to that of CHG, showing a negative correlation with gene expression (Figure 4d).

The relationship between gene-wide DNA methylation and expression

After exploring the relationship between methylation level in intron/exon and gene expression, we extended our analysis and considered the entire transcribed sequences defined as follows: 2 kb upstream of the TSS to 2 kb downstream of the TTS. Genes were divided into five categories according to expression levels (Figure S15). CG and CHG methylation around TSS and TTS decreased gradually with increasing gene expression (Figure 4e). Genes that were not expressed had high CG and CHG methylation levels in gene-body regions, and these levels were higher in flower tissues than in leaves (Figures 4e and S15). CG methylation inside gene bodies increased gradually in a bell-shaped manner with increasing expression (Figures 4e and S15). However, CHG methylation in gene bodies decreased with increasing transcript levels (Figures 4e,f and S16). CHH methylation around the TSS increased gradually with increasing expression (Figure 4e).

Methylation distribution in multi-exon genes

The high level of CG methylation in the center of gene bodies (Figure 2d), and higher CG methylation in introns than in exons (Figure 4d), promoted us to check whether methylation in introns might contribute to this local enrichment (Figure 2d). We divided genes into different categories according to the number of exons: one, two, three or four (Figure 5a). Single-exon genes had no enrichment of CG methylation marks towards the center of transcripts

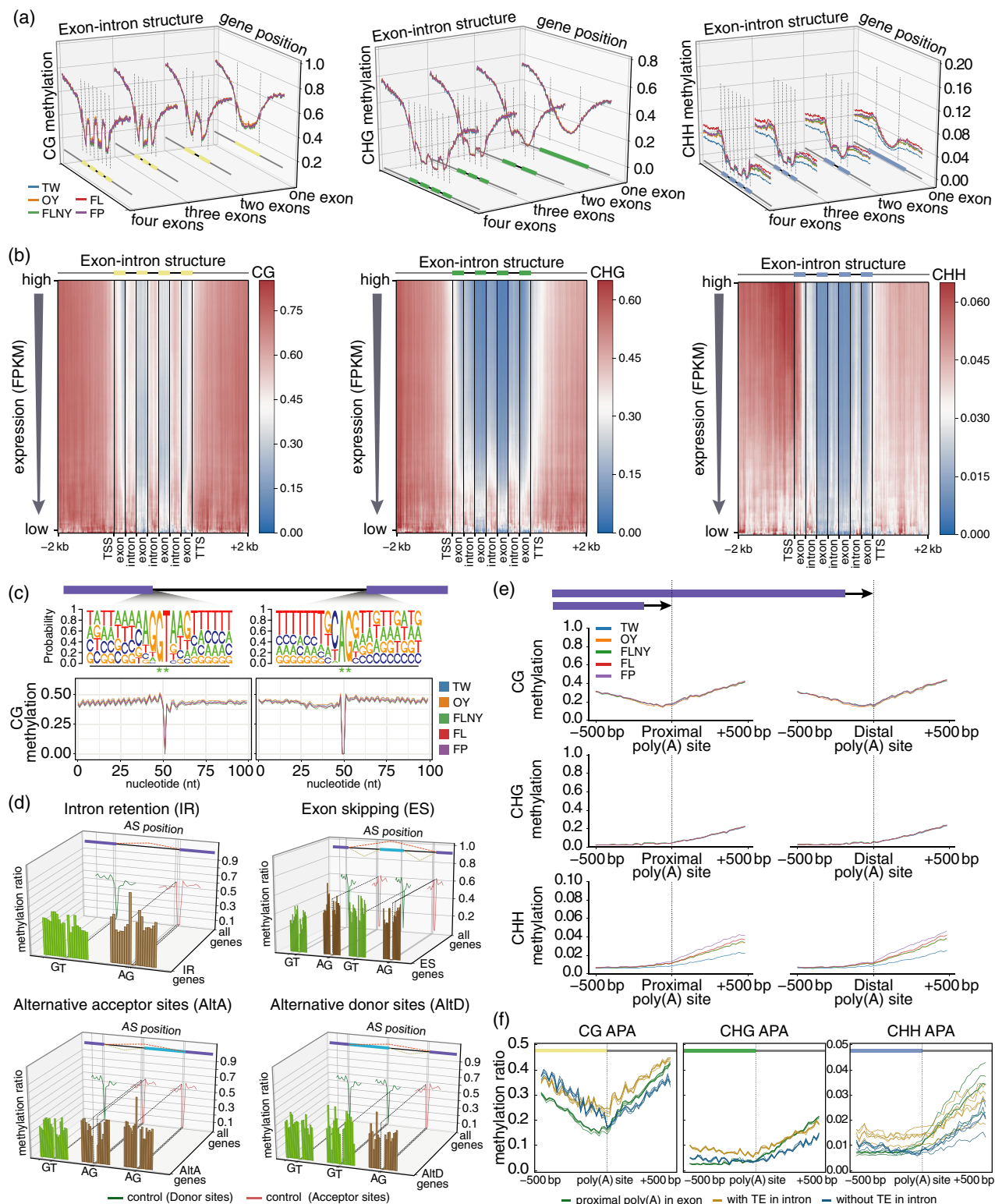


Figure 5. Overall distribution of methylation levels for multiple-exonic genes.

- (a) Overall distribution of methylation levels for genes with one, two, three or four exons.
 (b) Heatmaps representing the overall distribution of methylation levels in flowering plant (FL) samples for genes with four exons.
 (c) CG methylation with single-base resolution around splice donor sites (GT) and acceptor sites (AG).
 (d) CG methylation with single-base resolution around splicing sites from differential alternative splicing (AS) events.
 (e) Methylation profiles around distal and proximal poly(A) sites.
 (f) Methylation profiles of ± 500 bp around poly(A) sites in exons and in introns, with or without transposable elements (TEs).

(Figure 5a). For genes including two or more exons, CG methylation in introns was much higher than that in exons, indicating that the CG peak in the gene-body region was caused by high methylation in introns. CHG and CHH methylation also followed this trend. However, the difference in CHG and CHH methylation between exon and intron was not so pronounced as that for CG methylation. The first and last exons had slightly higher methylation levels than those in the middle (Figure 5a). Methylation levels within the first exons gradually decreased from TSS to the 3' end. Correspondingly, methylation levels for the last exons gradually increased from the 5' site to the TTS (Figure 5a).

For single-exon genes, higher expression was accompanied by lower CG methylation in the middle region of the single exon (Figure S17). A similar trend was observed for CHG and CHH methylation. For most multi-exonic genes, the CG, CHG and CHH methylation levels decreased in the first and in the last exon with increasing gene expression (Figure S17). CG methylation in introns was higher than that in exons (Figure 5b). Overall, CG and CHG methylation in introns decreased with increasing gene expression (Figures 5b and S17). However, this trend was less pronounced for CHH methylation marks (Figure 5b). In summary, DNA methylation within different transcribed regions plays different roles in the contribution to gene expression.

Methylation levels around splicing and polyadenylation sites

Single-base methylation analysis around splicing sites showed that CG methylation around donor sites was approximately 50%. As methylation occurred on cytosine residues, the sites without any methylation in the distribution curve were the thymine and adenine bases from donor and acceptor sites, respectively (Figure 5c). Although the overall methylation in introns was higher than in exons, the methylation around splicing sites in the flanking exon was slightly higher than in the flanking intron. However, CHG or CHH methylation levels around splicing sites in flanking exons were similar to those in flanking introns (Figure S18). Here, we mainly investigated the associations of methylation with four types of differential AS events (Figure S18). Methylation profiles around these different AS events revealed both hypermethylation and hypomethylation around splicing sites (Figure 5d).

Alternative polyadenylation (APA) included proximal poly(A) sites and distal poly(A) sites. Methylation distribution was similar at proximal and distal poly(A) sites (Figure 5e). We focused on different classes of proximal poly(A) sites based on their location in introns or exons. Using PacBio Iso-Seq full-length transcripts from our previous data (Wang *et al.*, 2017), we grouped poly(A) sites into three groups: proximal poly(A) within exons; proximal

poly(A) located in introns without TEs; and proximal poly(A) in TE-containing introns (Figure 5f). In the case of poly(A) sites in exons, CG methylation had decreasing levels upstream of the TTS and continued downstream with an upward trend. CG methylation for poly(A) sites in introns with a transposon was significantly higher downstream of poly(A) sites than upstream, indicating that transposons in introns were mainly located downstream of the poly(A) sites (Figure 5f). CHG methylation levels around poly(A) sites in exons were generally low and had a tendency to increase gradually downstream of the poly(A) cleavage sites (Figure 5f). Overall, CHG methylation levels around APA sites in the vicinity of TEs were higher than in the absence of nearby TEs (Figure 5f). CHH methylation was more variable but followed similar patterns as CHG methylation (Figure 5f). In summary, methylation in the vicinity of poly(A) sites in TE-containing introns was higher than in other poly(A) sites, which suggests that APA might be regulated by an epigenetic mark from intronic TE insertion.

Flanking introns of circular RNA are highly methylated

To investigate whether methylation patterns correlate with the transcription of circRNAs, we identified circRNA sequences genome wide using the same samples used for the methylation analysis. In this study, we used the high-purity circular RNA isolation (RPAD) method with a minor modification to identify circRNAs (Figure 6a). These circRNA-enriched samples were used for downstream library construction and sequencing. We identified a total of 1043 circular RNAs (Figure 6b). In all five libraries, most of the circular RNAs were formed by exon sequences. Next, we validated the accuracy of circRNA sequencing by RNase R treatment (Figure 6c). Through inverted complementary sequences in flanking introns of circRNA were reported to be involved in the biogenesis of circRNAs in mammalian cell (Chen, 2016; Wilusz, 2015). However, very few inverted complementary sequences were detected around the circularized exons in moso bamboo (Figure S19). This result suggests that the biogenesis of circRNA in moso bamboo does not depend on flanking complementary sequences, which is consistent with previous findings from *Arabidopsis* (Ye *et al.*, 2015) and *O. sativa* (Lu *et al.*, 2015a). We noticed that flanking introns around exons transcribed to circRNAs were highly methylated. For example, chromatin-remodeling factor (PH01000286G1030) generated circRNA, and its flanking introns showed high methylation densities (Figure 6d). We observed a similar pattern at the genome-wide level, with levels of methylation in flanking introns reaching more than 90% in some cases (Figure 6e). This level was similar to that seen at TEs, suggesting that TEs contributed to hypermethylation in flanking introns. Indeed, both upstream and downstream flanking introns included more TEs than on average (Figure 6f). siRNAs silence transposons through RdDM mechanisms (Gent

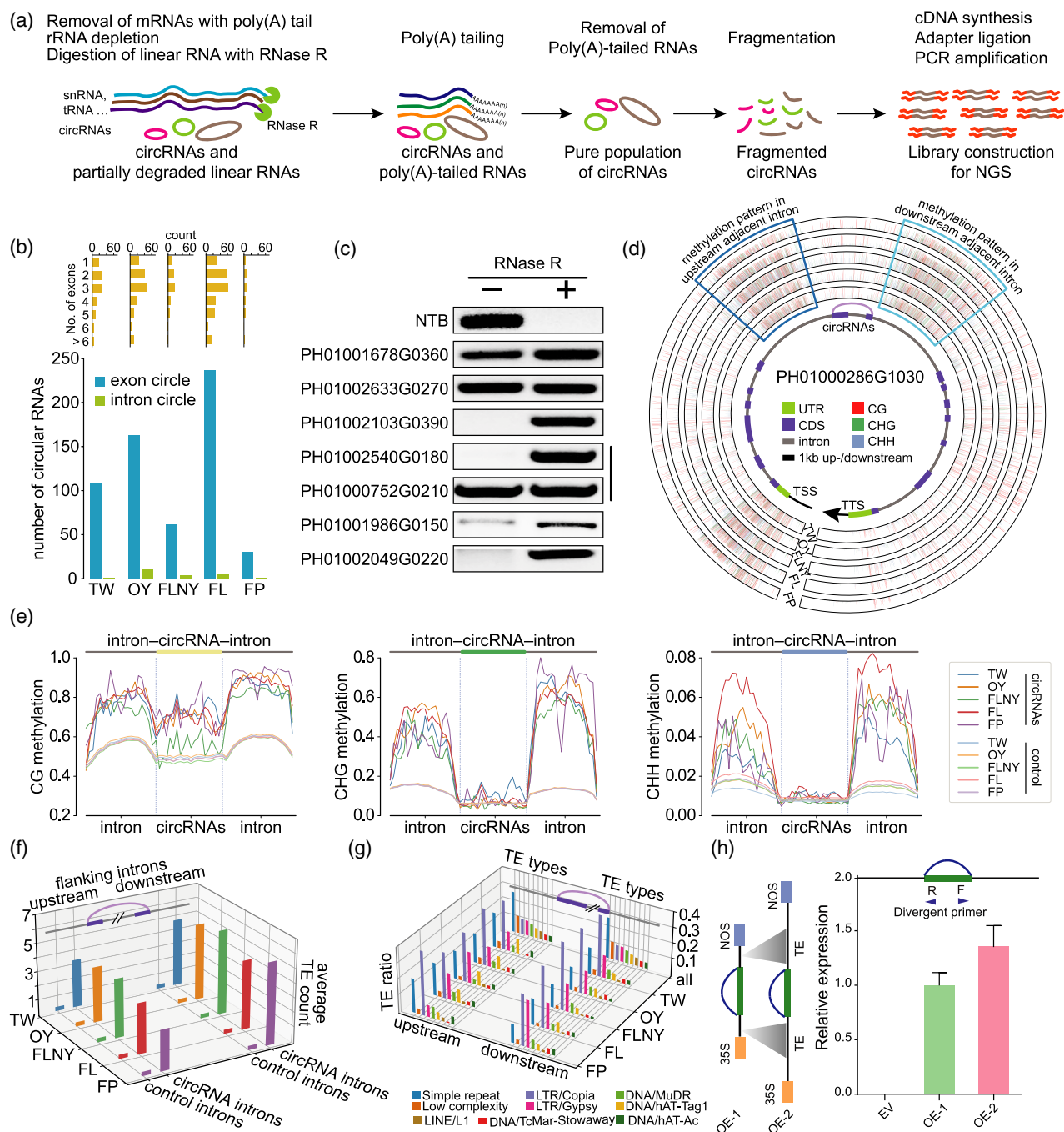


Figure 6. The relationship between DNA methylation and circRNA biogenesis.

(a) Flowchart for the construction of circRNA sequencing libraries.

(b) Total number of circRNAs identified in 3-week-old seedlings (TW), 1-year-old plants (OY), plants that will flower in the next year (FLNY), flowering plants (FL) and flower florets (FP).

(c) Validation of circRNAs using RNase R treatment experiment.

(d) Methylation landscape along the transcript of CRT1-like GHKL ATPase (*PH01000088G0990*) and identification of hypermethylated region in flanking introns of circRNA encoding exons.

(e) Methylation patterns around flanking introns of circRNAs.

(f) Average transposable element (TE) count in flanking introns of circRNA loci.

(g) TE types in flanking introns of circRNAs.

(h) Schematic structure of two different circular overexpression vectors, OE-1 and OE-2, representing vectors without and with TE (LTR/Copia), respectively. Quantitative real-time polymerase chain reaction (qRT-PCR) with divergent primers to detect expression of circular RNA derived from *PHO1000306G0430* in different overexpression systems.

et al., 2013). We noticed a trend for 24-nt siRNAs to be enriched in the flanking introns of circRNAs (Figure S20), which suggested that 24-nt siRNAs might specifically guide *de novo* methylation of the flanking introns of circRNAs. The classification of these TEs indicated that long terminal repeats (LTRs) were the most common type in the flanking introns of circRNAs (Figure 6g). To test whether and which type of TEs can be identified in different experimental conditions, we reanalyzed our previously published circRNA collection from rapidly growing shoots of moso bamboo (Wang *et al.*, 2019). Most of the previously identified circRNAs also showed TE enrichment in flanking introns, suggesting that TEs (LTR types) are involved in circRNA biogenesis (Figure S21). We further used comprehensive circular RNAs from PlantcircBase (Chu *et al.* 2017) to perform the same TE analysis in both *O. sativa* and *Z. mays*, which are in the Gramineae family. Two species also presented more TEs in flanking introns of circular RNAs (Figure S22), which suggested that TE correlated with circular RNA biogenesis might be an evolutionarily conserved mechanism in Gramineae. In order to verify the relationship between transposon and circular RNA biogenesis, we constructed two overexpressed vectors of circular RNA derived from *PH01000306G0430* with (OE-2) and without (OE-1) TE. The recombinant plasmid was transformed into protoplasts of moso bamboo separately, with a transformation efficiency of approximately 40%, using PEG-mediated protoplast transfection. We observed that in the presence of TE (OE-2) the expression level of circular RNA was higher than that in the absence of TE (Figure 6h), indicating that TE in the flanking intron might affect the abundance of circular RNA, as an important *cis*-regulated element. However, *trans*-acting factors might also regulate the biogenesis of circular RNAs in different stages. Thus, we expect new knowledge about the biogenesis of circular RNA using cross-linking immunoprecipitation (HITS-CLIP, also known as CLIP-Seq) in the future (Zhang *et al.*, 2015).

DISCUSSION

Here, we present the first report of a single-base-resolution methylome in moso bamboo. Methylome changes across different periods in moso bamboo development allowed us to study correlations between DNA methylation and chronological age. The genome-wide single-base-resolution methylation profile showed that methylation at CG and CHG was more stable with age than methylation at CHH. The CHH methylation level in TEs and annotated genes gradually accumulated from vegetative to reproductive growth. CHH methylation was not only highly variable, but also tissue and age specific, so can potentially be used as a signature of aging. These observations are in agreement with previous studies (Lister *et al.*, 2013). For instance, a study in mice revealed that age could be predicted with an absolute error of 3.33 weeks based on 329

CG sites (Stubbs *et al.*, 2017). In plants, environmental factors could influence the accumulation of methylated cytosine at different CG sites (Jiang *et al.*, 2014), which provides an additional challenge. In theory, old tissues would accumulate more methylation changes than young tissues. In this study, we included five different stages to identify conserved or unique epigenetic changes associated with age. Moso bamboo is a perennial plant species, which might be subject to various abiotic and biotic stresses during long flowering intervals. Thus, some of the DMRs could be caused by environmental factors. However, synchronized flowering in different regions can only be explained by a dominant internal physiological calendar overriding external environmental cues (Franklin, 2004; Janzen, 1976). Thus, most of the DMRs in this study are likely to come from the internal epigenetic clock associated with chronological age. Cytokinin can induce flowering *in vitro* in *Bambusa arundinacea* (clump bamboo) (Joshi and Nadgauda, 1997). However, we were not able to induce flowering in moso bamboo, which is a scattered bamboo (Figure S23). Flower regulation might differ between clump bamboo and scattered bamboo, and in the case of moso bamboo might depend to a larger extent on an internal physiological calendar, which is more resistant to external hormone treatments.

In addition to 5mC, the presence of DNA methylation on *N*⁶-adenine (6mA) has been confirmed in plants (Karanthamalai *et al.* 2020). 6mA has been identified in Arabidopsis with a greater than 100-fold coverage of the genome based on PacBio SMRT sequencing (Liang *et al.* 2018). The modification can be identified by raw signal data from nanopore sequencing in *Drosophila* based on a 6mA model in TOMBO (Shah *et al.* 2019). In this study, we validated BS-Seq using single-molecule nanopore DNA sequencing by sequencing an approximately 2× coverage of bamboo genome, which did not present enough coverage to reliably identify 6mA. Whether 6mA is relevant to the phase transition in bamboo will be an interesting epigenetics mechanism for further investigation.

The regulation of APA by methylation has remained unclear so far in plants. In this study, proximal and distal poly(A) sites showed similar DNA methylation profiles. TEs reside in the atypically large introns of *FLC* (Liu *et al.*, 2004) and *IBM1* (Rigal *et al.*, 2012). At the same time, 3' distal polyadenylation sites from genes with methylated intronic TEs could be promoted by two anti-silencing factors: EDM2 (Lei *et al.*, 2014) and ASI1 (Wang *et al.*, 2013). Thus, we focused on one type of special poly(A) site, which resided in introns. The level of methylation in introns with poly(A) sites was significantly higher downstream of the poly(A) sites, indicating that downstream transposons might affect poly(A) site usage. After checking three Arabidopsis genes from previous reports, we found that 3'-proximal poly(A) sites from two genes (*AT3G05410* and

AT1G11270) were located mainly in the 5' region of intronic TEs (Wang *et al.*, 2013). This result is consistent with the methylation profile in this study, which suggests that it might be a conserved regulatory mechanism in both monocots and dicots.

In this study, we further investigated the relationship between expression and methylation. CG and CHG methylation around TSS and TTS decreased gradually with increasing gene expression levels. CHH methylation correlates, to a certain degree, with gene expression, especially when located in the promoter region of genes. In addition to promoter and TSS/TTS, this study also revealed the importance of the outermost exons on gene expression. In different tissues, we observed large methylation changes of genes that were not expressed and hypermethylation in both promoter and gene body regions (Figure 4e). Surprisingly, CG methylation in introns was higher than in exons. CHG and CHH methylation in intron or exon regions decreased with increasing expression. GO enrichment analysis of CG DMR-containing genes among different chronological ages showed obvious enrichment in 'vegetative to reproductive phase transition of meristem', which suggested a link between DNA methylation and flowering.

Understanding the networks of the master floral developmental regulator is necessary to get the full picture of the phase transition in moso bamboo in the future. Although the function of SOC1 and FT are well characterized in model plant species (Lee and Lee 2010), how the master floral developmental regulator activated flowering remains unknown in bamboo. In this study, *SOC1* demonstrated low expression at the leaf of early juvenile stage (TW/OY) and high expression at the reproductive stage (FLNY/FL) (Figure S24). *SOC1*, encoding a MADS-box protein, is regulated by age-related *SPL9* (Wang *et al.* 2009). *SPL9* presented low expression in TW and gradually increased in OY and FLNY (Figure S23), which was consistent with the role of age-related positive regulation of SOC1. In addition to *SOC1*, FT is another flowering pathway integrator (Lee and Lee 2010). In moso bamboo, FT demonstrated the highest expression level in the FL stage, consistent with a role in regulating flowering as an upstream activator of *SOC1*. At present, transformation technology for moso bamboo is not yet available. Developing efficient regeneration and transformation methods for moso bamboo will be essential for future research. Overexpression or mutation of the above-mentioned genes could then be applied to further study their potential roles in triggering phase transitions in moso bamboo.

By combining genome-wide circRNA-Seq analysis with BS-Seq, we revealed that flanking introns of circRNAs were densely methylated and enriched for TEs. Our result is consistent with a previous study in maize, which showed an enrichment of LINE1-like elements and their reverse

complementary pairs in the flanking regions of circRNAs (Chen *et al.*, 2018). Although it is well known that circRNAs originate from back-splicing (Zhang *et al.*, 2016), it is not clear how TEs might stimulate circRNA production. Previous studies reported that DNA methylation could regulate the splicing of linear transcription (Dujardin *et al.*, 2014; Maor *et al.*, 2015). Thus, a first possibility is that the high level of DNA methylation in introns causes a reduction in the RNA polymerase II elongation rate, in order to regulate the back-splicing of circRNA biogenesis. A second possibility is that epigenetic factors bind to the flanking intron regions and compete with splicing factors to affect circRNA biogenesis. For instance, in *Arabidopsis*, *INCREASE IN BONSAI METHYLATION 2* (*IBM2*) is needed for the DNA hypermethylation of gene bodies (Saze *et al.*, 2013). Although *IBM2* does not affect RNA polymerase II elongation, *IBM2* contains the bromo-adjacent homology domain that probably binds to an RNA recognition motif (Taiko *et al.*, 2015). Thus, epigenetic factors like *IBM2* might bind to the hypermethylated region in flanking introns and compete with splicing factors to regulate back-splicing. At present, DNA methyltransferase mutants are not available because of the lack of an efficient regeneration and transformation protocol for moso bamboo. In the future, studying circRNA biogenesis in different DNA methyltransferase mutant backgrounds using high-efficiency transformation might reveal a role for DNA methylation in circRNA biogenesis in plants.

EXPERIMENTAL PROCEDURES

Morphology and scanning electron microscopy analysis

A Canon EOS 70D digital camera (Canon, <https://global.canon>) was used to document the phenotypes of leaves and flower panicles at distinct growth stages. Detailed images of flower florets were collected under a Leica M205FA stereomicroscope (Leica Microsystems, <https://www.leica-microsystems.com>). Trichomes on the edge and adaxial epidermis of leaves at distinct growth stages and epidermal cells of flower panicles were observed using a TM3030 tabletop scanning electron microscope (Hitachi, <https://www.hitachi.com>). We selected six bulliform cells and arm cells for each leaf and calculated the area with IMAGEJ (<https://imagej.nih.gov/ij>) using 10 leaves. After staining, slices were observed with the Leica DM6B microscope and the leaf thickness was measured using IMAGEJ. Data were statistically analyzed using two-way analysis of variance (ANOVA).

Cytological observations and measurement of chlorophyll content

The middle of the leaves was cut into pieces with double-sided razor blades, and subsequently cleared with lactic acid saturated with chloral hydrate at 70°C for 1 h. Leaf sections were transferred to a glass slide after washing three times with distilled water. The sections were stained for 15 sec using staining solution, which was prepared by diluting 1% Toluidine Blue O solution (cat. no. G3663; Solarbio, <http://www.solarbio.net>) to 0.01% with 20% ethanol. Cytological observations were carried

out using a Leica DM6B microscope after washing twice (Lux *et al.*, 2005).

To estimate the chlorophyll content, 0.1 g of leaf material, excluding midribs, was cut into pieces followed by immersion in a 10-ml mixture of ethanol, acetone and distilled water (4.5:4.5:1, v/v/v). After incubation at room temperature (22–25°C) in the dark for 3 days, the sample turned white. Then, 3 ml of the clear supernatant was transferred to a 10-mm cuvette to measure the optical density at 645 and 663 nm with a UV1200 spectrophotometer (Mapada, <https://mapada.en.ecplaza.net>). Chlorophyll concentrations were calculated using Arnon's equations: $(20.21 \times A_{645} + 8.02 \times A_{663}) \times (V/W)$ (Arnon, 1949), with at least three replicates.

Bisulfite sequencing and bioinformatic analysis

Genomic DNA was isolated using the Plant Genomic DNA Kit (cat. no. DP305-02; Tiangen, <https://en.tiangen.com>). Bisulfite conversion was carried out with the EZ DNA Methylation-Gold kit (Zymo Research, <https://www.zymoresearch.com>) following the manufacturer's protocol. After library construction, paired-end reads were generated on a HiSeq X Ten sequencing platform (Illumina, <https://www.illumina.com>) with a genome coverage of about 30×. Using the genome sequence of moso bamboo (Zhao *et al.*, 2014), BISMAR was used to report alignments as BAM files using default parameters and the methylated reference genome created by BISMAR_GENOME_PREPARATION (Krueger and Andrews, 2011). Then methylation information was extracted using BISMAR_METHYLATION_EXTRACTOR, with the following options: `-p --no_overlap --comprehensive --report --bedGraph --CX_context --scaffolds --cytosine_report`. DMRcaller (Catoni *et al.*, 2018) with default parameters was used to identify DMRs, defined as <100 bp and with methylation differences of 0.4, 0.2 and 0.1 for CG, CHG and CHH, respectively.

Single-molecule nanopore DNA sequencing and bioinformatic analysis

Genomic DNA (gDNA) libraries from TW and FL were sequenced according to the protocol SQK-LSK108 by Oxford Nanopore Technologies (ONT, <https://nanoporetech.com>). Input gDNA samples were quantified using a Qubit 2.0 fluorometer and the Qubit dsDNA HS Assay Kit (cat. no. Q32851; ThermoFisher Scientific, <https://www.thermoFisher.com>). Nuclease-free water (NFW) was added to adjust 1.5 µg of high-molecular-weight genomic DNA samples to 45 µl. The input gDNA sample was repaired and end-prepped by NEBNext FFPE DNA Repair Mix (cat. no. M6630; NEB, <https://www.neb.com>) and NEBNext Ultra II End Repair/dA-tailing Module (cat. no. E7546; NEB), respectively. The repaired gDNA was washed with 70% freshly prepared ethanol and cleaned using 1× Agencourt AMPure XP beads (cat. no. A63880; Beckman Coulter, <https://www.beckmancoulter.com>). Adapter Mix (SQK-LSK108; ONT) and Blunt/TA Ligase Master Mix (cat. no. M0367; NEB) were used for sequencing adapter ligation. The final purification of the adapted gDNA library was performed using adapter bead binding (SQK-LSK108; ONT) to remove the free adapter and 0.4× Agencourt AMPure XP beads. The final purified gDNA sample was eluted with 15 µl of NFW and a 1-µl elution was quantified (recovery aim ≥430 ng) using the Qubit method mentioned above. The pre-sequencing mix (PSM) was prepared by mixing the gDNA library with running buffer with fuel mix (SQK-LSK108; ONT), library loading beads (SQK-LSK108; ONT) and NFW, then loaded onto an R9.4.1 FlowCell (FLO-MIN106; ONT) and run on a MinION MK1B instrument (ONT) for 48 h.

In the Nanopore sequencing file, FAST5 was converted into a single file with the `multi_to_single_fast5` from https://github.com/nanoporetech/ont_fast5_api. Then the script of `read_fast5_basecaller.py` from ALBACORE 1.2.x (ONT) was used to do base calling for each FAST5 file for subsequent analysis. TOMBO (<https://nanoporetech.github.io/tombo>) was used for data processing and extraction of the methylation file. In brief, a genomic index file was generated using the `resquiggle` command in TOMBO. 5mC methylation was identified using the `tombo detect_modifications alternative_model`. Finally, the coordinates of methylated sites were extracted using `tomb text_output browser_files --statistics-filename --file-types dampened_fraction --browser-file`. The whole bioinformatics analysis was written in PYTHON script analysis. The graphics were plotted using matplotlib and seaborn PYTHON libraries (<http://matplotlib.org>).

RNA-Seq and small RNA sequencing and bioinformatics analysis

Total RNAs were extracted from tissues with the RNeasy Pure Plant Kit (cat. no. DP441; Tiangen). Strand-specific RNA-Seq libraries were constructed as described previously by dUTP strand-specific library protocol (Wang *et al.*, 2017). In brief, fragments of approximately 400–500 nt in length were selected and isolated from a 2% agarose gel. Then dUTP libraries were sequenced using an Illumina HiSeq 2500 platform to generate 125-nt paired-end reads, which were mapped to the moso bamboo genome using TOPHAT 2.0.11 with the following options: `--read-mismatches 5 --read-gap-length 5 --read-edit-dist 5 -p 10 -r 50 -a 8` (Trapnell *et al.*, 2009) with an anchor length more than 8 nt. The above alignment files were further assembled using CUFFLINKS 2.1.1 (Trapnell *et al.*, 2012) with the following options: `-F 0.05 -A 0.01 -l 100000 --min-intron-length 30`. Assembled transcripts and the RNA-Seq aligned reads were loaded into RMA 3.2.2 (Shen *et al.*, 2014) using the following parameters: `-t paired -len 125 -a 8 -c 0.0001 -analysis U`. Differential AS events were defined with $P < 0.05$. Differential expression genes were identified using EDGER (Robinson *et al.*, 2010), defined by a fold change of >1.5 and a false discovery rate (FDR) of <0.05. Small RNA libraries were constructed following a previous method (Wang *et al.*, 2019). The adapter sequences were cleaned using the FASTX toolkit (http://hannonlab.cshl.edu/fastx_toolkit/). Then all small RNA reads were aligned with the reference genome using BOWTIE 2.2.1 (Langmead and Salzberg, 2012). The values of small RNAs were normalized using read per million (RPM).

Co-expression networks and GO enrichment analysis

Differentially expressed genes were used to construct co-expression networks with the R package WGCNA (Langfelder and Horvath, 2008). First, differentially expressed genes with CG, CHG and CHH contexts were used separately to generate co-expression networks using WGCNA in R (Langfelder and Horvath, 2008). The parameters for each network were identical. The adjacency matrix was constructed using the `adjacency()` function with the parameters `power = 22`, `method = 'spearman'` and `type = 'signed'`. Topographical overlap matrices (TOMs) were measured as edge weights using the `TOMsimilarity()` function with default parameters. From the TOMs every possible pair of bamboo genes was calculated to get the Spearman's rank correlation coefficient, which was sorted from high to low, for choosing the top 10% gene pairs. Finally, the top 10% gene pairs were merged into unique gene sets and the frequency of each unique gene from these gene pairs was calculated to choose the top 10% genes for hub gene analysis.

We functionally annotated each gene in moso bamboo using BLAST2GO (Conesa *et al.*, 2005), which provided functional information based on the function of homologs in model plant species. In particular, 96 genes related to the vegetative–reproductive phase transition of the meristem were annotated.

Construction of circular RNA library for Illumina sequencing and bioinformatic analyses

Firstly, poly(A)– RNAs were separated using the Dynabeads mRNA Purification kit (cat. no. 61006; Invitrogen, now ThermoFisher Scientific, <https://www.thermofisher.com>). A standard agarose gel, loading equal quantities of PCR products from the *actin* gene, including the poly(A) tail, validated the effect of poly(A)+ RNA depletion (Data S1; Figures S25a). Ribosomal RNA (rRNA) was depleted from poly(A)– RNAs using the RiboMinus™ Plant Kit for RNA-Seq (cat. no. A1083808; Invitrogen, now ThermoFisher Scientific). Agarose gel electrophoresis from 18S and 28S rRNA further validated the effects of rRNA depletion (Figure S25b). The above poly(A)–/Ribo– RNAs were digested with 3 µl of 10× RNase R Reaction Buffer and 1.5 µl of RNase R (20 U µl^{−1}) at 37°C for 15 min. Primers from linear transcripts validated the depletion of linear RNAs by RNase R (Figure S25c). Then the Poly(A) tailing kit (cat. no. AM1350; Invitrogen, now ThermoFisher Scientific) and RiboLock RNase inhibitor (ThermoFisher Scientific) were mixed with 20 µl of RNase R-treated RNA and incubated at 37°C for 30 min to add poly(A) tails to residual linear transcripts. Finally, circRNAs were enriched from the 40-µl reaction mixture after a second-round depletion of linear fragments with oligo(T) beads. CircRNA primers were used to validate the existence of circRNAs (Figure S25d).

Clean reads were aligned with the genome using TOPHAT 2.0.11 with the following parameters: -a 6 -microexon -m 2 (Trapnell *et al.*, 2009). The remaining unmapped reads were realigned with the reference genome using TOPHAT-FUSION 2.0.11 with the following parameters: -fusion-search -keep-fasta-order -bowtie1 -no-coverage-search -r 0 -mate-std-dev 80 -max-intron-length 100 000 -fusion-min-dist 100 000 -fusion-anchor-length 20 (Kim and Salzberg, 2011) to obtain reads mapped to back-splicing junction sites. CircRNAs were then predicted using CIRCEXPLOER with default options (Zhang *et al.*, 2014). The abundance of circRNAs was evaluated by RPM (reads mapped to back-splicing junctions per million mapped reads).

Overexpression of circular RNA

Vectors without and with TE (LTR/Copia) were transformed into protoplasts from moso bamboo using PEG-mediated protoplast transfection, as previously described (Wang *et al.*, 2019).

ACKNOWLEDGEMENTS

This work was supported by the National Key Research and Development Program of China (2018YFD0600101), the National Natural Science Foundation of China Grant (grant nos 31971734, 31570674 and 31800566), the Distinguished Young Scholar Program of Fujian Agriculture and Forestry University (grant no. xjq202017) and the Program for Scientific and Technological Innovation Team in University of Fujian Province (grant no. 118/KLA18069A). SEJ is an investigator of the Howard Hughes Medical Institute. We thank Dr Katrina Woolcock from Life Science Editors for her editing work.

CONFLICT OF INTEREST

The authors declare that they have no competing interests associated with this work.

AUTHOR CONTRIBUTIONS

LG and SEJ conceived and designed the research. LG, QZ, YZ, BL, AA and YH managed the project. ZZ, Y-SW, H-YW, MVK, YG and HZ performed the bioinformatics. H-HW, FX, PG, WW, KC, XL, XH and KH performed experiments. ZZ, SEJ and LG wrote the article.

DATA AVAILABILITY STATEMENT

Raw sequencing data have been submitted to the NCBI Gene Expression Omnibus under accession numbers GSE122135, GSE121216 and GSE139217. Related data generated for this study are available at forestry.fafu.edu.cn/pub/bamboo_flower.

SUPPORTING INFORMATION

Additional Supporting Information may be found in the online version of this article.

Figure S1. Measurement of the cell size of bulliform cell, arm cell and the thickness of leaves in TW, OY, FLNY and FL, respectively.

Figure S2. Correlations among different biological replicates.

Figure S3. The x-axis presents leaves of differing chronological age. The y-axis presented CHH methylation level. The *P* value from pairwise comparisons were labeled in the figures.

Figure S4. Correlation between distance between TE pairs and methylation level of TE interval region. The y-axis shows the methylation level of the TE interval region. The x-axis shows distance (50 bp bin^{−1} for 30 bins) between two neighboring TEs.

Figure S5. GO term enrichment analysis of DMR genes.

Figure S6. Heatmap of normalized expression values for all genes associated with the vegetative to reproductive phase transition.

Figure S7. GO term enrichment analysis for downregulated (a) and upregulated (b) genes.

Figure S8. Co-expression networks of RNA-Seq.

Figure S9. GO term enrichment analysis for each co-expressed module during phase transition.

Figure S10. The GO term enrichment analysis of constructed networks.

Figure S11. Scatter plots showing the relationship between promoter methylation (y-axis) and expression level (x-axis).

Figure S12. Distribution of 24-nt siRNAs situated both 1 kb upstream and downstream of TSS and TTS, respectively. Four quartiles (low, mid-low, mid-high, high) were classified based on the CHH methylation level in 1-kb regions of both upstream and downstream of TSS and TTS, respectively. The x-axis presented the coordinate information. The y-axis presented normalized 24-nt siRNA.

Figure S13. The expression of DNA methyltransferase DRM2 in each library shown upregulation in flowering samples. (a) The expression (FPKM) of DNA methyltransferase DRM2 based on RNA-Seq. (b) Quantification of DRM2 in five samples of moso bamboo using quantitative real-time PCR.

Figure S14. The histogram represented the total number of CG nucleotides in annotated exon and intron, respectively. The outside circle represented percentage of CG nucleotides in exon and intron, respectively. Right panel shown the modified CG number in five samples.

Figure S15. CG, CHG, and CHH methylation profiles in genes from high to low expression. DNA methylation landscape was

presented in genes from high expression (a), moderate to low (b-d) and no expression (e) groups, respectively.

Figure S16. CG, CHG and CHH methylation heatmaps for genes ordered by expression level from low to high.

Figure S17. CG, CHG and CHH methylation heatmaps for single and multi-exon genes ordered by expression level from low to high.

Figure S18. DNA methylation around splicing sites and statistics of differential AS events. (a) CHG and CHH methylation around splicing sites (GT-AG) at single-base resolution. (b) Differential AS events of four pairwise comparisons.

Figure S19. The percentage of circular RNAs with and without flanking inverted complementary intron sequences, depicted in brown and blue, respectively.

Figure S20. Enrichment of siRNA in flanking intron of circular RNAs. All annotated introns were selected as the control group. The y-axis represented normalized small RNA coverage; 24-nt siRNA in intron of flanking circRNAs presented higher abundance than control group.

Figure S21. TE types in flanking introns of circRNAs from fast growing shoots.

Figure S22. TE in flanking introns of circRNAs from *Oryza sativa* and *Zea mays*, respectively.

Figure S23. *In vitro*-induced flowering in moso bamboo: (a) 5-month-old bamboo plants were grown on MS basic medium without any addition of plant growth hormones; (b) when MS basal medium was supplemented with 0.5 mg L⁻¹ 6-BA and 0.25 mg L⁻¹ IBA, multiple shoots at the base were observed; (c) MS basal medium supplemented with 1.0 mg L⁻¹ TDZ; (d) MS basal medium supplemented with 0.5 mg L⁻¹ 6-BA, 0.25 mg L⁻¹ IBA and 0.5 mg L⁻¹ GA3, leading to multiple branches at internodes. Compared with (b), GA3 was more beneficial for shoot formation. (e) MS basal medium supplemented with 0.8 mg L⁻¹ TDZ. Low concentration of TDZ is more conducive to the occurrence of multiple shoots. (f) MS basal medium supplemented with 5 mg L⁻¹ 6-BA. In the presence of higher concentration of 6-BA, multiple shoots occurred at the internodes of bamboo, and the growth state was better.

Figure S24. The expression of important master floral developmental regulator such as SOC1 and FT.

Figure S25. Construction of circular RNA library. (a) RT-PCR validation of poly(A-) RNA isolation. The same quantity of total RNA, poly(A)+ RNA, poly(A)- RNA was reverse transcribed with oligoT primer. Actin was selected as linear transcript marker with polyadenylated tail. (b) Validation of subsequent rRNA depletion. The same quantity of total RNA, poly(A)- RNA, poly(A)-/ribo-RNA was loaded on a 1% agarose gel. It showed that 28S and 18S ribosomal RNAs were efficiently removed after rRNA depletion. (c) RT-PCR validation of RNase R digestion. Circular RNAs remained stable, whereas the linear RNA was degraded after RNase R treatment. (d) Detection of circular RNAs and linear RNA in the final RNA sample. Note that the linear RNA cannot be detected but circular RNAs still exist.

Data S1. Details of primer sequences for experimental validation and vector construction.

REFERENCES

- Annon, D.I. (1949) Copper enzymes in isolated chloroplasts. Polyphenoloxidase in *Beta vulgaris*. *Plant Physiology*, **24**, 1.
- Ay, N., Janack, B. & Humbeck, K. (2014) Epigenetic control of plant senescence and linked processes. *Journal of Experimental Botany*, **65**, 3875–3887.
- Catoni, M., Tsang, J.M., Greco, A.P. & Zabet, N.R. (2018) DMRcaller: a versatile R/Bioconductor package for detection and visualization of differentially methylated regions in CpG and non-CpG contexts. *Nucleic Acids Research*, **46**, e114.
- Chan, S.W., Henderson, I.R. & Jacobsen, S.E. (2005) Gardening the genome: DNA methylation in *Arabidopsis thaliana*. *Nature Reviews Genetics*, **6**, 351–360.
- Chen, G., Cui, J., Wang, L., Zhu, Y., Lu, Z. & Jin, B. (2017) Genome-wide identification of circular RNAs in *Arabidopsis thaliana*. *Frontiers in Plant Science*, **8**, 1678.
- Chen, L.L. (2016) The biogenesis and emerging roles of circular RNAs. *Nature Reviews Molecular Cell Biology*, **17**, 205–211.
- Chen, L., Zhang, P., Fan, Y., Lu, Q., Li, Q., Yan, J. *et al.* (2018) Circular RNAs mediated by transposons are associated with transcriptomic and phenotypic variation in maize. *New Phytologist*, **217**, 1292–1306.
- Christiansen, L., Lenart, A., Tan, Q., Vaupel, J.W., Aviv, A., McGue, M. *et al.* (2016) DNA methylation age is associated with mortality in a longitudinal Danish twin study. *Aging Cell*, **15**, 149–154.
- Chu, Q., Zhang, X., Zhu, X., Liu, C., Mao, L., Ye, C. *et al.* (2017) Plantcirc-Base: a database for plant circular RNAs. *Molecular plant*, **10**, 1126–1128.
- Conesa, A., Gotz, S., Garcia-Gomez, J.M., Terol, J., Talon, M. & Robles, M. (2005) Blast2GO: a universal tool for annotation, visualization and analysis in functional genomics research. *Bioinformatics*, **21**, 3674–3676.
- Conn, V.M., Hugouvieux, V., Nayak, A., Conos, S.A., Capovilla, G., Cildir, G. *et al.* (2017) A circRNA from SEPALLATA3 regulates splicing of its cognate mRNA through R-loop formation. *Nature Plants*, **3**, 17053.
- Du, J., Johnson, L.M., Jacobsen, S.E. & Patel, D.J. (2015) DNA methylation pathways and their crosstalk with histone methylation. *Nature Reviews Molecular Cell Biology*, **16**, 519–532.
- Dubrovina, A.S. & Kiselev, K.V. (2016) Age-associated alterations in the somatic mutation and DNA methylation levels in plants. *Plant Biology*, **18**, 185–196.
- Dujardin, G., Lafaille, C., de la Mata, M., Marasco, L.E., Munoz, M.J., Le Jossic-Corcoss, C. *et al.* (2014) How slow RNA polymerase II elongation favors alternative exon skipping. *Molecular Cell*, **54**, 683–690.
- Franklin, D.C. (2004) Synchrony and asynchrony: observations and hypotheses for the flowering wave in a long-lived semelparous bamboo. *Journal of Biogeography*, **31**, 773–786.
- Gent, J.I., Ellis, N.A., Guo, L., Harkess, A.E., Yao, Y., Zhang, X. *et al.* (2013) CHH islands: de novo DNA methylation in near-gene chromatin regulation in maize. *Genome Research*, **23**, 628–637.
- Godoy Herz, M.A., Kubaczka, M.G., Brzyzek, G., Servi, L., Krzysztos, M., Simpson, C. *et al.* (2019) Light regulates plant alternative splicing through the control of transcriptional elongation. *Molecular Cell*, **73**, 1066–1074.e1063.
- Hannum, G., Guinney, J., Zhao, L., Zhang, L., Hughes, G., Sadda, S. *et al.* (2013) Genome-wide methylation profiles reveal quantitative views of human aging rates. *Molecular Cell*, **49**, 359–367.
- Hsu, F.M., Yen, M.R., Wang, C.T., Lin, C.Y., Wang, C.R. & Chen, P.Y. (2017) Optimized reduced representation bisulfite sequencing reveals tissue-specific mCHH islands in maize. *Epigenetics Chromatin*, **10**, 42.
- Humbeck, K. (2013) Epigenetic and small RNA regulation of senescence. *Plant Molecular Biology*, **82**, 529–537.
- Janzen, D.H. (1976) Why bamboos wait so long to flower. *Annual Review of Ecology Systematics*, **7**, 347–391.
- Jeck, W.R., Sorrentino, J.A., Wang, K., Slevin, M.K., Burd, C.E., Liu, J. *et al.* (2013) Circular RNAs are abundant, conserved, and associated with ALU repeats. *RNA*, **19**, 141–157.
- Jiang, C., Mithani, A., Belfield, E.J., Mott, R., Hurst, L.D. & Harberd, N.P. (2014) Environmentally responsive genome-wide accumulation of de novo *Arabidopsis thaliana* mutations and epimutations. *Genome Research*, **24**, 1821–1829.
- Joshi, M. & Nadgauda, R.S. (1997) Cytokinins and in vitro induction of flowering in bamboo: *Bambusa arundinacea* (Retz.) Willd. *Current Science*, **73**, 523–526.
- Karanthamalai, J., Chodon, A., Chauhan, S. & Pandi, G. (2020) DNA N6-methyladenine modification in plant genomes—A glimpse into emerging epigenetic code. *Plants*, **9**, 247.
- Kim, D. & Salzberg, S.L. (2011) TopHat-Fusion: an algorithm for discovery of novel fusion transcripts. *Genome Biology*, **12**, R72.

- Krueger, F. & Andrews, S.R. (2011) Bismark: a flexible aligner and methylation caller for Bisulfite-Seq applications. *Bioinformatics*, **27**, 1571–1572.
- Langfelder, P. & Horvath, S. (2007) Eigengene networks for studying the relationships between co-expression modules. *BMC systems biology*, **1**, 1–17.
- Langfelder, P. & Horvath, S. (2008) WGCNA: an R package for weighted correlation network analysis. *BMC Bioinformatics*, **9**, 559.
- Langmead, B. & Salzberg, S.L. (2012) Fast gapped-read alignment with Bowtie 2. *Nature Methods*, **9**, 357–359.
- Law, J.A. & Jacobsen, S.E. (2010) Establishing, maintaining and modifying DNA methylation patterns in plants and animals. *Nature Reviews Genetics*, **11**, 204–220.
- Lee, J. & Lee, I. (2010) Regulation and function of SOC1, a flowering pathway integrator. *Journal of Experimental Botany*, **61**, 2247–2254.
- Lei, M., La, H., Lu, K., Wang, P., Miki, D., Ren, Z. et al. (2014) Arabidopsis EDM2 promotes IBM1 distal polyadenylation and regulates genome DNA methylation patterns. *Proceedings of the National Academy of Sciences of the United States of America*, **111**, 527–532.
- Li, H., Freeling, M. & Lisch, D. (2010) Epigenetic reprogramming during vegetative phase change in maize. *Proceedings of the National Academy of Sciences of the United States of America*, **107**, 22184–22189.
- Li, L., Hu, T., Li, X., Mu, S., Cheng, Z., Ge, W. et al. (2016) Genome-wide analysis of shoot growth-associated alternative splicing in moso bamboo. *Molecular Genetics and Genomics*, **291**, 1695–1714.
- Li, Q., Gent, J.I., Zynda, G., Song, J., Makarevitch, I., Hirsch, C.D. et al. (2015) RNA-directed DNA methylation enforces boundaries between heterochromatin and euchromatin in the maize genome. *Proceedings of the National Academy of Sciences of the United States of America*, **112**, 14728–14733.
- Liang, Z., Shen, L., Cui, X., Bao, S., Geng, Y., Yu, G. et al. (2018) DNA N6-adenine methylation in *Arabidopsis thaliana*. *Developmental Cell*, **45**, 406–416.
- Lin, X., Chow, T., Chen, H.-H., Liu, C., Chou, S., Huang, B. et al. (2010) Understanding bamboo flowering based on large-scale analysis of expressed sequence tags. *Genetics and Molecular Research*, **9**, 1085–1093.
- Lister, R., Mukamel, E.A., Nery, J.R., Urich, M., Puddifoot, C.A., Johnson, N.D. et al. (2013) Global epigenomic reconfiguration during mammalian brain development. *Science*, **341**, 1237905.
- Liu, J., He, Y., Amasino, R. & Chen, X. (2004) siRNAs targeting an intronic transposon in the regulation of natural flowering behavior in Arabidopsis. *Genes & Development*, **18**, 2873–2878.
- Lu, T., Cui, L., Zhou, Y., Zhu, C., Fan, D., Gong, H. et al. (2015) Transcriptome-wide investigation of circular RNAs in rice. *RNA*, **21**, 2076–2087.
- Lux, A., Morita, S., Abe, J. & Ito, K. (2005) An improved method for clearing and staining free-hand sections and whole-mount samples. *Annals of Botany*, **96**, 989–996.
- Maor, G.L., Yearim, A. & Ast, G. (2015) The alternative role of DNA methylation in splicing regulation. *Trends in Genetics*, **31**, 274–280.
- Maunakea, A.K., Chepelev, I., Cui, K. & Zhao, K. (2013) Intragenic DNA methylation modulates alternative splicing by recruiting MeCP2 to promote exon recognition. *Cell Research*, **23**, 1256–1269.
- Miura, F., Enomoto, Y., Daijiri, R. & Ito, T. (2012) Amplification-free whole-genome bisulfite sequencing by post-bisulfite adaptor tagging. *Nucleic Acids Research*, **40**, e136.
- Niederhuth, C.E., Bewick, A.J., Ji, L., Alabady, M.S., Kim, K.D., Li, Q. et al. (2016) Widespread natural variation of DNA methylation within angiosperms. *Genome Biology*, **17**, 194.
- Numata, M. (1970) Conservational implications of bamboo flowering and death in Japan. *Biological Conservation*, **2**, 227–229.
- Ogneva, Z., Dubrovina, A. & Kiselev, K. (2016) Age-associated alterations in DNA methylation and expression of methyltransferase and demethylase genes in *Arabidopsis thaliana*. *Biologia Plantarum*, **60**, 628–634.
- Pavlopoulou, A. & Kossida, S. (2007) Plant cytosine-5 DNA methyltransferases: structure, function, and molecular evolution. *Genomics*, **90**, 530–541.
- Peng, Z., Lu, Y., Li, L., Zhao, Q., Feng, Q., Gao, Z. et al. (2013) The draft genome of the fast-growing non-timber forest species moso bamboo (*Phyllostachys heterocycla*). *Nature Genetics*, **45**, 456.
- Penterman, J., Zilberman, D., Huh, J.H., Ballinger, T., Henikoff, S. & Fischer, R.L. (2007) DNA demethylation in the Arabidopsis genome. *Proceedings of the National Academy of Sciences of the United States of America*, **104**, 6752–6757.
- Rigal, M., Kevei, Z., Péliissier, T. & Mathieu, O. (2012) DNA methylation in an intron of the IBM1 histone demethylase gene stabilizes chromatin modification patterns. *The EMBO Journal*, **31**, 2981–2993.
- Robinson, M.D., McCarthy, D.J. & Smyth, G.K. (2010) edgeR: a Bioconductor package for differential expression analysis of digital gene expression data. *Bioinformatics*, **26**, 139–140.
- Saze, H., Kitayama, J., Takashima, K., Miura, S., Harukawa, Y., Ito, T. et al. (2013) Mechanism for full-length RNA processing of Arabidopsis genes containing intragenic heterochromatin. *Nature Communications*, **4**, 1–9.
- Shah, K., Cao, W. & Ellison, C.E. (2019) Adenine methylation in *Drosophila* is associated with the tissue-specific expression of developmental and regulatory genes. *G3: Genes, Genomes, Genetics*, **9**, 1893–1900.
- Shen, S., Park, J.W., Lu, Z.X., Lin, L., Henry, M.D., Wu, Y.N. et al. (2014) rMATS: robust and flexible detection of differential alternative splicing from replicate RNA-Seq data. *Proceedings of the National Academy of Sciences of the United States of America*, **111**, E5593–E5601.
- Shukla, S., Kavak, E., Gregory, M., Imashimizu, M., Shutinoski, B., Kashlev, M. et al. (2011) CTCF-promoted RNA polymerase II pausing links DNA methylation to splicing. *Nature*, **479**, 74–79.
- Simpson, J.T., Workman, R.E., Zuzarte, P., David, M., Dursi, L. & Timp, W. (2017) Detecting DNA cytosine methylation using nanopore sequencing. *Nature Methods*, **14**, 407–410.
- Singh, A., Zubko, E. & Meyer, P. (2008) Cooperative activity of DNA methyltransferases for maintenance of symmetrical and non-symmetrical cytosine methylation in *Arabidopsis thaliana*. *The Plant Journal*, **56**, 814–823.
- Stubbs, T.M., Bonder, M.J., Stark, A.-K., Krueger, F., von Meyenn, F., Stegle, O. et al. (2017) Multi-tissue DNA methylation age predictor in mouse. *Genome Biology*, **18**, 68.
- Susan, J.C., Harrison, J., Paul, C.L. & Frommer, M. (1994) High sensitivity mapping of methylated cytosines. *Nucleic Acids Research*, **22**, 2990–2997.
- Taiko, K.T., Saze, H. & Kakutani, T. (2015) DNA methylation within transcribed regions. *Plant Physiology*, **168**, 1219–1225.
- Takahashi, M., Furusawa, H., Limtong, P., Sunanthapongsuk, V., Marod, D. & Panuthai, S. (2007) Soil nutrient status after bamboo flowering and death in a seasonal tropical forest in western Thailand. *Ecological Research*, **22**, 160–164.
- Trapnell, C., Pachter, L. & Salzberg, S.L. (2009) TopHat: discovering splice junctions with RNA-Seq. *Bioinformatics*, **25**, 1105–1111.
- Trapnell, C., Roberts, A., Goff, L., Pertea, G., Kim, D., Kelley, D.R. et al. (2012) Differential gene and transcript expression analysis of RNA-seq experiments with TopHat and Cufflinks. *Nature Protocols*, **7**, 562–578.
- Vijg, J. & Suh, Y. (2013) Genome instability and aging. *Annual Review of Physiology*, **75**, 645–668.
- Vo, J.N., Cieslik, M., Zhang, Y., Shukla, S., Xiao, L., Zhang, Y. et al. (2019) The landscape of circular RNA in cancer. *Cell*, **176**, 869–881.e13.
- Wachter, A., Tunc-Ozdemir, M., Grove, B.C., Green, P.J., Shintani, D.K. & Breaker, R.R. (2007) Riboswitch control of gene expression in plants by splicing and alternative 3' end processing of mRNAs. *The Plant Cell*, **19**, 3437–3450.
- Wang, T., Wang, H., Cai, D., Gao, Y., Zhang, H., Wang, Y. et al. (2017) Comprehensive profiling of rhizome-associated alternative splicing and alternative polyadenylation in moso bamboo (*Phyllostachys edulis*). *The Plant Journal*, **91**, 684–699.
- Wang, J.-W., Czech, B. & Weigel, D. (2009) miR156-regulated SPL transcription factors define an endogenous flowering pathway in *Arabidopsis thaliana*. *Cell*, **138**, 738–749.
- Wang, X., Duan, C.G., Tang, K., Wang, B., Zhang, H., Lei, M. et al. (2013) RNA-binding protein regulates plant DNA methylation by controlling mRNA processing at the intronic heterochromatin-containing gene IBM1. *Proceedings of the National Academy of Sciences of the United States of America*, **110**, 15467–15472.
- Wang, X., Hu, L., Wang, X., Li, N., Xu, C., Gong, L. et al. (2016) DNA methylation affects gene alternative splicing in plants: an example from rice. *Molecular Plant*, **9**, 305–307.
- Wang, Y., Gao, Y., Zhang, H., Wang, H., Liu, X., Xu, X. et al. (2019) Genome-wide profiling of circular RNAs in the rapidly growing shoots of moso bamboo (*Phyllostachys edulis*). *Plant and Cell Physiology*, **60**, 1354–1373.

- Wilusz, J.E. (2015) Repetitive elements regulate circular RNA biogenesis. *Mobile Genetic Elements*, **5**(3), 39–45.
- Wu, J., Qi, X., Liu, L., Hu, X., Liu, J., Yang, J. *et al.* (2019) Emerging epigenetic regulation of circular RNAs in human cancer. *Molecular Therapy - Nucleic Acids*, **16**, 589–596.
- Ye, C.Y., Chen, L., Liu, C., Zhu, Q.H. & Fan, L. (2015) Widespread noncoding circular RNAs in plants. *New Phytologist*, **208**, 88–95.
- Yearim, A., Gelfman, S., Shayevitch, R., Melcer, S., Glaich, O., Mallm, J.P. *et al.* (2015) HP1 is involved in regulating the global impact of DNA methylation on alternative splicing. *Cell Reports*, **10**, 1122–1134.
- Yuan, J.-L., Sun, H.-M., Guo, G.-P., Yue, J.-J. & Gu, X.-P. (2014) Correlation between DNA methylation and chronological age of Moso bamboo (*Phyllostachys heterocycla* var. *pubescens*). *Botanical Studies*, **55**, 4.
- Zampieri, M., Ciccarone, F., Calabrese, R., Franceschi, C., Bürkle, A. & Caiafa, P. (2015) Reconfiguration of DNA methylation in aging. *Mechanisms of Ageing and Development*, **151**, 60–70.
- Zhang, H., Lang, Z. & Zhu, J.-K. (2018) Dynamics and function of DNA methylation in plants. *Nature Reviews Molecular Cell Biology*, **19**, 489–506.
- Zhang, P., Fan, Y., Sun, X., Chen, L., Terzaghi, W., Bucher, E. *et al.* (2019a) A large-scale circular RNA profiling reveals universal molecular mechanisms responsive to drought stress in maize and Arabidopsis. *The Plant Journal*, **98**, 697–713.
- Zhang, X.-O., Dong, R., Zhang, Y., Zhang, J.-L., Luo, Z., Zhang, J. *et al.* (2016) Diverse alternative back-splicing and alternative splicing landscape of circular RNAs. *Genome Research*, **26**, 1277–1287.
- Zhang, X.O., Wang, H.B., Zhang, Y., Lu, X.H., Chen, L.L. & Yang, L. (2014) Complementary sequence-mediated exon circularization. *Cell*, **159**, 134–147.
- Zhang, X., Zhang, Y., Wang, T., Li, Z., Cheng, J., Ge, H. *et al.* (2019b) A comprehensive map of intron branchpoints and lariat RNAs in plants. *The Plant Cell*, **31**, 956–973.
- Zhang, Y., Gu, L., Hou, Y., Wang, L., Deng, X., Hang, R. *et al.* (2015) Integrative genome-wide analysis reveals HLP1, a novel RNA-binding protein, regulates plant flowering by targeting alternative polyadenylation. *Cell Research*, **25**, 864–876.
- Zhao, H., Peng, Z., Fei, B., Li, L., Hu, T., Gao, Z. *et al.* (2014) (2014) BambooGDB: a bamboo genome database with functional annotation and an analysis platform. *Database*, **2014**, bau006.
- Zhao, L., Zhang, H., Kohnen, M.V., Prasad, K.V., Gu, L. & Reddy, A.S. (2019) Analysis of transcriptome and epitranscriptome in plants using PacBio Iso-Seq and nanopore-based direct RNA sequencing. *Frontiers in Genetics*, **10**, 253.
- Zhu, J.K. (2009) Active DNA demethylation mediated by DNA glycosylases. *Annual Review of Genetics*, **43**, 143–166.